Modeling, validation, and performance of low-frequency piezoelectric energy harvesters

Abdelkefi, A.; Barsallo, Nilma; Tang, Lihua; Yang, Yaowen; Hajj, Muhammad R

2014

Abdelkefi, A., Barsallo, N., Tang, L., Yang, Y., & Hajj, M. R. (2014). Modeling, validation, and performance of low-frequency piezoelectric energy harvesters. Journal of intelligent material systems and structures, 25(12), 1429-1444.

https://hdl.handle.net/10356/101679

https://doi.org/10.1177/1045389X13507638

Modeling, Validation, and Performance of Low-Frequency Piezoelectric Energy Harvesters

A. Abdelkefi[1], **N. Barsallo**[1], **L. Tang**[2], **Y. Yang**[2], **and M. R. Hajj**[1]

[1] *Department of Engineering Science and Mechanics, MC 0219, Virginia Tech, Blacksburg, Virginia 24061, USA.*

[2] *School of Civil and Environmental Engineering, Nanyang Technological University, 50 Nanyang Avenue, Singapore 639798.*

Abstract

Analytical and finite element electromechanical models that take into account the fact that the piezoelectric sheet does not cover the whole substrate beam are developed. A linear analysis of the analytical model is performed to determine the optimal load resistance. The analytical and finite element models are validated with experimental measurements. The results show that the analytical model that takes into account the fact that the piezoelectric patch does not cover the whole beam predicts accurately the experimental measurements. The finite element results yield a slight discrepancy in the global frequency and a slight overestimation in the value of the harvested power at resonance. On the other hand, using an approximate analytical model based on mode shapes of the full covered beam leads to erroneous results and overestimation of the global frequency as well as the

Email address: abdes09@vt.edu, Phone number: +15402097083 Fax:+15402314574 (**A. Abdelkefi**[1])

level of harvested power. In order to design enhanced piezoelectric energy harvesters that can generate energy at low frequency excitations, further analysis is performed to investigate the effects of varying the length of the piezoelectric material on the natural frequency and the performance of the harvester. The results show that there is a compromise between the length of the piezoelectric material, the electrical load resistance, and the available excitation frequency. By quantifying this compromise, we optimize the performance of beam-mass systems to efficiently harvest energy from a specified low-frequency of the ambient vibrations.

Keywords: Energy harvesting, Piezoelectric material, Low-frequency, Distributed-parameter model, Finite element analysis.

1. Introduction

Different structural systems for energy harvesting from ambient or aeroelastic vibrations have been proposed (Erturk et al., 2010; Sousa et al., 2010; Abdelkefi et al., 2012a; Daqaq, 2012; Abdelkefi et al., 2012b, 2013). These systems vary from simple beam and beam-mass systems to more complex structures, such as zigzag and spiral systems (Karami and Inman, 2011). The purpose for these variations is to enable harvesting energy at specific frequencies. One advantage for using unimorph piezoelectric beam-mass systems for energy harvesting from ambient vibrations is their simple configuration and design and optimal performance. An issue, however, has been the accurate modeling of these simple devices which is required for efficient design. Such modeling is required because when operating in their linear regime, piezoelectric beam-mass harvesters will only be able to efficiently

harvest energy over a narrow range of frequencies. Missing this range of frequencies will result in significantly reduced harvested power. Roundy and Wright (2005) and DuToil et al. (2005) modeled a piezoelectric cantilever beam as a mass-spring-damper system. Such a model is limited to the fundamental frequency of the structure and does not account for the effects of the dynamic mode shapes on the electrical response of the harvester. The effect of the spring mass (distributed mass) was not considered in the forcing amplitude. This assumption fails in cases where the proof mass is small. Erturk and Inman (2008) showed that the use of the traditional form of the lumped-parameter model leads to erroneous results for both transverse and longitudinal cantilevered beams under base vibrations. They showed that the predicted response can be underestimated when using the conventional effective mass of cantilevered beams or bars. This is particularly true when there is a small or no tip mass. As such, they introduced correction factors to improve the prediction capability of lumped models for harmonic base excitation for both transverse and longitudinal vibrations. Improved models that are based on the Galerkin discretization were used in different studies (Erturk and Inman, 2008, 2009; Abdelkefi et al., 2011, 2012c; Masana and Daqaq, 2011; Ben Ayed et al., 2013). This method is more accurate in comparison to the lumped-parameter models. This approach takes into consideration the effects of the dynamic mode shapes, strain distribution and higher vibration modes on the electromechanical response of the harvester.

A common problem, when basing a reduced-order model for piezoelectric energy harvesters on the Galerkin approximation, is the determination of the mode shapes and natural frequencies. The classical mode shapes of a

fully-covered piezoelectric cantilever beam is usually assumed for experiments where the piezoelectric material does not cover the whole substrate beam (Song et al., 2009, 2010; Masana and Daqaq, 2011; Alamin et al., 2012; Hobeck and Inman, 2012). In this work, we improve the prediction capability by deriving an analytical electromechanical model of a beam-mass energy harvester with a piezoelectric patch that does not cover the whole substrate beam. The exact mode shapes and natural frequencies using the derived analytical model, approximate analytical model (determined by assuming a fully-covered beam), and finite element analysis results are compared with experimental measurements. Furthermore, linear analysis of the analytical models is performed to investigate the effects of the load resistance on the fundamental global frequency and the harvester's response. The validation of the different methods is performed through comparison with experimental measurements. To design enhanced harvesters that can generate energy at low frequency excitations, a parametric study is conducted to investigate the effects of varying the length of the piezoelectric material on the mode shapes, natural frequencies, and the performance of the harvester.

2. Representation of the used models and experimental setup

2.1. Analytical models

2.1.1. Global electromechanical modeling

We consider the problem of harvesting energy from a directly excited unimorph piezoelectric cantilever beam with a tip mass. The cantilever beams consist of aluminum and piezoelectric layers and is subjected to direct excitation, as shown in Figure 1. The piezoelectric layers are bounded by

two-in-plane electrodes of negligible thicknesses connected to an electrical load resistance. These electrodes are assumed to be perfectly conductive and cover the entire piezoelectric surface. We assume that the thickness of the beam is small compared to its length so that the shear deformation and rotary inertia can be neglected. The clamped end of the beam is subjected to a transverse harmonic displacement $Y(t) = Y_0 cos(\Omega t)$.

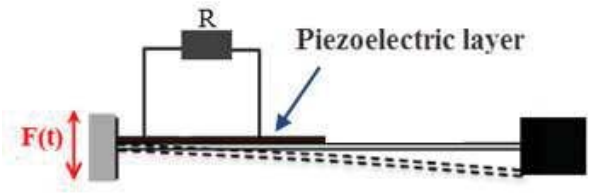

Figure 1: A schematic of the piezoelectric energy harvester under direct excitation

By modeling this bi-layered cantilever beam as an Euler-Bernoulli beam, the partial differential equation governing its relative transverse vibration $v = v(x,t)$ when subjected to direct excitation is written as

$$\frac{\partial^2 M(x,t)}{\partial x^2} + c_a \frac{\partial v(x,t)}{\partial t} + m\frac{\partial^2 v(x,t)}{\partial t^2} = -[m + M_t\delta(x-L)]\frac{\partial^2 Y(t)}{\partial t^2} + M_t L_c \frac{d\delta(x-L)}{dx}\frac{\partial^2 Y(t)}{\partial t^2} \quad (1)$$

where $\delta(x)$ is the Dirac delta function, L is the length of the substrate beam, L_c is half the the length of the tip mass, c_a is the viscous air damping coefficient, m is the mass of the beam per unit length, M_t is the tip mass, and $M(x,t)$ is the internal moment which has three components (Erturk and Inman, 2008). The first of these components is the resistance to bending and

is given by $EI\frac{\partial^2 v(x,t)}{\partial x^2}$. The second component is due to strain rate damping effect and is represented by $c_s I\frac{\partial^3 v(x,t)}{\partial x^2 \partial t}$. The third component is the contribution of the unimorph piezoelectric layer. This contribution is represented by $\vartheta_p(H(x-L_1)-H(x-L_2))V(t)$ where $H(x)$ is the Heaviside step function, $V(t)$ is the generated voltage, L_1 is the distance from the left end of cantilever beam to the starting location of the piezoelectric layer, L_2 is the distance from the left end of cantilever beam to the ending location of the piezoelectric layer and ϑ_p is the piezoelectric coupling term. This term is given by (Erturk and Inman, 2008; Abdelkefi et al., 2011, 2012c)

$$\vartheta_p = -e_{31} b_2 \frac{(y_1+y_2)}{2} \tag{2}$$

where $e_{31} = E_p d_{31}$ is the piezoelectric stress coefficient, b_2 is the width of the piezoelectric layer and y_1 and y_2 are the positions of the layers with respect to the neutral axis, as shown in Figure 2, $\bar{y} = \frac{(h_p+h_s)E_p h_p}{2(E_p h_p + E_s h_s)} + \frac{h_s}{2}$ and are related as follows:

$$y_0 = -\bar{y}\ ,\ y_1 = h_s - \bar{y}\ ,\ y_2 = (h_s+h_p) - \bar{y}$$

where h_s and h_p are the thicknesses of the aluminum and piezoelectric layers, respectively. E_s and E_p are the respective Young's Modulus of these layers.

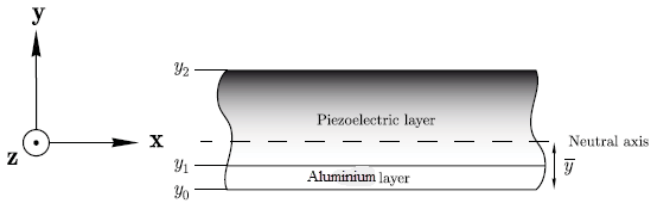

Figure 2: Neutral axis position.

Substituting the moment $M(x,t)$ in equation (1) by its three components, the governing equation of motion of the electromechanical system is written as

$$EI\frac{\partial^4 v(x,t)}{\partial x^4} + c_s I\frac{\partial^5 v(x,t)}{\partial x^4 \partial t} + c_a\frac{\partial v(x,t)}{\partial t} + m\frac{\partial^2 v(x,t)}{\partial t^2} + (\frac{d\delta(x-L_1)}{dx} - \frac{d\delta(x-L_2)}{dx})\vartheta_p V(t) = -[m + M_t\delta(x-L)]\frac{\partial^2 Y(t)}{\partial t^2} + M_t L_c\frac{d\delta(x-L)}{dx}\frac{\partial^2 Y(t)}{\partial t^2} \quad (3)$$

where the stiffness EI and mass of the beam per unit length m are given by:

$EI = EI_1 = \frac{1}{12}b_1 E_s {h_s}^3$ and $m = m_1 = b_1\rho_s h_s$ for $0 \le x < L_1$ or $L_2 < x \le L$

and

$EI = EI_2 = \frac{1}{3}E_s b\,(y_1^3 - y_0^3) + \frac{1}{3}E_p b\,(y_2^3 - y_1^3)$ and $m = m_2 = b_1\rho_s h_s + b_2\rho_p h_p$ for $L_1 \le x \le L_2$

where ρ_s and ρ_p are the densities of the aluminum and piezoelectric layers, respectively.

To relate the mechanical and electrical components, we use the Gauss law (IEEE, 1987)

$$\frac{d}{dt}\int_A \mathbf{D}.\mathbf{n}\; dA = \frac{d}{dt}\int_A D_3\; dA = \frac{V}{R} \quad (4)$$

where $\mathbf{D}$ is the electric displacement vector and $\mathbf{n}$ is the normal vector to the plane of the beam. The electric displacement component D_3 is given by the following relation (Erturk and Inman, 2009):

$$D_3(x,t) = e_{31}\varepsilon_{11}(x,t) + \epsilon_{33}^s E_3 \quad (5)$$

where ε_{11} is the axial strain component in the aluminum and piezoelectric layers and is given by $\varepsilon_{11}(x,y,t) = -y\frac{\partial^2 v(x,t)}{\partial x^2}$, ϵ_{33}^s is the permittivity component at constant strain. Substituting (5) into (4), we obtain the equation governing the strain-voltage relation (Erturk and Inman, 2008):

$$-e_{31}\frac{(y_1+y_2)}{2}b_2\int_{L_1}^{L_2}\frac{\partial^3 v(x,t)}{\partial t\partial x^2}dx-\frac{\epsilon_{33}^s b_2(L_2-L_1)}{h_p}\frac{dV(t)}{dt}=\frac{V(t)}{R} \quad (6)$$

2.1.2. Eigenvalue problem analysis

To perform the linear analysis, we discretize the system using the Galerkin procedure which requires the exact mode shapes of the structure. These mode shapes are determined by dropping the damping, forcing, and polarization from equation (3), and letting $v(x,t)=\phi(x)e^{i\omega t}$. Because the piezoelectric layer does not cover the whole cantilever beam, we divide the mode shape into three different regions:

$\phi(x)=\phi_1(x)$ for $0\leq x<L_1$

$\phi(x)=\phi_2(x)$ for $L_1\leq x\leq L_2$

$\phi(x)=\phi_3(x)$ for $L_2<x\leq L$

The resulting eigenvalue problem for each region is given by

$$EI_1\phi_1^{iv}-m_1\omega^2\phi_1=0 \quad (7)$$

$$EI_2\phi_2^{iv}-m_2\omega^2\phi_2=0 \quad (8)$$

$$EI_1\phi_3^{iv}-m_1\omega^2\phi_3=0 \quad (9)$$

with the boundary conditions

$$\phi_1(0) = 0 \ , \ \phi_1{}'(0) = 0 \ , \ \phi_1(L_1) = \phi_2(L_1); \tag{10}$$

$$\phi_1{}'(L_1) = \phi_2{}'(L_1) \ , \ EI_1\phi_1{}''(L_1) = EI_2\phi_2{}''(L_1) \tag{11}$$

$$EI_1\phi_1{}'''(L_1) = EI_2\phi_2{}'''(L_1) \ , \ \phi_2(L_2) = \phi_3(L_2) \ , \ \phi_2{}'(L_2) = \phi_3{}'(L_2) \tag{12}$$

$$EI_2\phi_2{}''(L_2) = EI_1\phi_3{}''(L_2) \ , \ EI_2\phi_2{}'''(L_2) = EI_1\phi_3{}'''(L_2) \tag{13}$$

$$EI_1\phi_3{}''(L) - \omega^2 M_t L_c \phi_3(L) - \omega^2(I_t + M_t L_c^2)\phi_3{}'(L) = 0 \tag{14}$$

$$EI_1\phi_3{}'''(L) + \omega^2 M_t \phi_3(L) + \omega^2 M_t L_c \phi_3{}'(L) = 0 \tag{15}$$

where I_t is the rotary inertia of the tip mass M_t at its center and L_c is half of the length of the tip mass. The mode shapes for the three different regions are then written as

$$\phi_1(x) = A_1 \sin\beta_1 x + B_1 \cos\beta_1 x + C_1 \sinh\beta_1 x + D_1 \cosh\beta_1 x \tag{16}$$

$$\phi_2(x) = A_2 \sin\beta_2 x + B_2 \cos\beta_2 x + C_2 \sinh\beta_2 x + D_2 \cosh\beta_2 x \tag{17}$$

$$\phi_3(x) = A_3 \sin\beta_1 x + B_3 \cos\beta_1 x + C_3 \sinh\beta_1 x + D_3 \cosh\beta_1 x \tag{18}$$

where the coefficients of β_1 and β_2 are related by $\beta_1 = \sqrt[4]{\frac{EI_2 m_1}{EI_1 m_2}}\beta_2$. Normalizing the eigenfunctions using the following orthogonality conditions yields the relation between the different coefficients in (10)-(15):

$$\int_0^{L_1} \phi_{1s}(x) m_1 \phi_{1r}(x) dx + \int_{L_1}^{L_2} \phi_{2s}(x) m_2 \phi_{2r}(x) dx \tag{19}$$
$$+ \int_{L_2}^{L_3} \phi_{3s}(x) m_1 \phi_{3r}(x) dx + \phi_{3s}(L) M_t \phi_{3r}(L) + \phi_{3s}'(L)(I_t + M_t L_c^2)\phi_{3r}'(L)$$
$$+ \phi_{3s}(L) M_t L_c \phi_{3r}'(L) + \phi_{3s}'(L) M_t L_c \phi_{3r}(L) = \delta_{rs}$$
$$\int_0^{L_1} \frac{d^2\phi_{1s}(x)}{dx^2} EI_1 \frac{d^2\phi_{1r}(x)}{dx^2} dx + \int_{L_1}^{L_2} \frac{d^2\phi_{2s}(x)}{dx^2} EI_2 \frac{d^2\phi_{2r}(x)}{dx^2} dx \tag{20}$$
$$+ \int_{L_2}^{L} \frac{d^2\phi_{3s}(x)}{dx^2} EI_1 \frac{d^2\phi_{3r}(x)}{dx^2} dx = \delta_{rs}\omega_r^2$$

where s and r are used to represent the vibration modes and δ_{rs} is the Kronecker delta, defined as unity when s is equal r and zero otherwise.

To derive a model of the considered energy harvester, we express the displacement $v(x,t)$ using the Galerkin procedure in the form

$$v(x,t) = \sum_{i=1}^{\infty} \phi_{ji}(x) q_i(t) \tag{21}$$

where j=1,2,3 depending on the value of x, $q_i(t)$ are the modal coordinates and $\phi_{ji}(x)$ are the mode shapes. Substituting equation (21) into equations (3) and (6) and considering one mode in the Galerkin approach, we obtain the following coupled equations of motions:

$$\ddot{q}(t) + 2\xi\omega\dot{q}(t) + \omega^2 q(t) + \chi V(t) = f(t) \tag{22}$$
$$C_p\dot{V}(t) + \frac{V(t)}{R} - \chi\dot{q}(t) = 0 \tag{23}$$

where ξ is the mechanical damping ratio (measured experimentally), ω is the fundamental natural frequency of the structure, the coefficients χ and C_p are the piezoelectric coupling term and the capacitance of the harvester

which are given by $\chi = (\phi_2'(L_2) - \phi_2'(L_1))\vartheta_p$ and $C_p = \frac{\epsilon_{33}^s b_2 (L_2 - L_1)}{h_p}$. $f(t)$ is the forcing term of the first mode which is given by: $f(t) = a[m_1 \int_0^{L_1} \phi_1(x)dx + m_2 \int_{L_1}^{L_2} \phi_2(x)dx + m_1 \int_{L_2}^{L} \phi_3(x)dx + M_t\phi_3(L) + M_t L_c \phi_3{}'(L)]cos(\Omega t) = Facos(\Omega t)$, where $a = Y_0\Omega^2$ is the base excitation and $F = m_1 \int_0^{L_1} \phi_1(x)dx + m_2 \int_{L_1}^{L_2} \phi_2(x)dx + m_1 \int_{L_2}^{L} \phi_3(x)dx + M_t\phi_3(L) + M_t L_c \phi_3{}'(L)$.

To determine closed form expressions for the tip deflection and the generated voltage, we assume that the base excitation can be expressed by $Y = Y_0 e^{i\Omega t}$, where Ω is the excitation frequency, and that $q = Qe^{i\Omega t}$ and $V = V_0 e^{i\Omega t}$. Equations (22) and (23) can then be written in the form

$$\begin{bmatrix} \omega^2 - \Omega^2 + 2i\xi\Omega & \chi \\ -i\chi\Omega & \frac{1}{R} + i\Omega C_p \end{bmatrix} \begin{bmatrix} Q \\ V_0 \end{bmatrix} = \Omega^2 Y_0 \begin{bmatrix} F \\ 0 \end{bmatrix}, \qquad (24)$$

The solution is obtained for the tip displacement $v(L,t) = \phi_3(L)Re(Qe^{i\Omega t})$ and the generated voltage V is determined by taking only the real part of the solution of Equation (24) ($V = Re(V_0 e^{i\Omega t})$) since we are assuming that $Y(t) = Y_0 \cos(\Omega t)$ which is the real part of the considered excitation. Finally, the electrical harvested power is computed as $P = \frac{V^2}{R}$.

To demonstrate the importance of considering different regions in the determination of the mode shapes, we consider another analytical model that is based on the classical mode shapes of a unimorph piezoelectric cantilever beam (fully covered). In this analysis, we determine the mode shapes of a fully covered piezoelectric cantilever beam and then we use the orthogonality conditions presented in equations (19) and (20) to normalize the equations of motion. We will refer to this model as approximate model.

2.2. Finite element electromechanical modeling

A finite element model was also developed to investigate the performance of the proposed piezoelectric energy harvester. The commercial software ANSYS was used to analyze this model as shown in Figure 3. In this electromechanical model, 3D 20-node structural solid element SOLID186 was applied for the aluminum beam and proof mass. Moreover, 3D 20-node coupled-field solid element SOLID226 was applied for the piezoelectric sheet. The voltage degree of freedom on the top and bottom surfaces were coupled to provide uniform electrical potentials and, thus, to emulate the electrodes of the piezoelectric sheet. First, the electrodes of the piezoelectric sheet were disconnected from the resistor and modal analysis was performed. The electrical potential of the bottom electrode of the piezoelectric sheet was set to zero. This analysis gives the open global frequency. Then, both electrodes were set to zero. This analysis provides the short global frequency. Subsequently, the two electrodes of the piezoelectric sheet were connected to the resistor by coupling the voltage degree of freedom of the electrodes and the two node of the resistor element, as shown in Figure 3. Instead of applying the displacement at the clamped boundary, a corresponding acceleration field due to base excitation was applied to the harvester. Harmonic analysis was then performed to obtain the steady-state power output.

2.3. Experimental setup

A prototype of the piezoelectric energy harvester was devised and tested. The experimental setup is shown in Figure 4. The harvester was composed of an aluminum cantilever beam bonded with a piezoelectric Macro Fiber Composite (MFC) at its root and a proof mass was attached to its free end. The

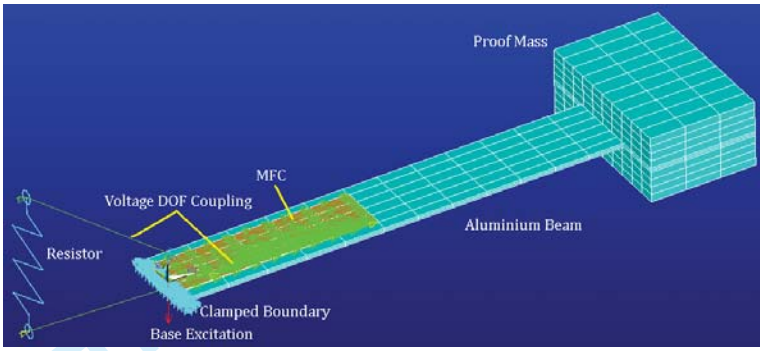

Figure 3: Finite element representation of the piezoelectric energy harvester

center of the proof mass was exactly located at the free end of the cantilever. The parameters of the devised piezoelectric energy harvester are given in Table 1. The sinusoidal drive signal was generated from a function generator and amplified before it was fed to the seismic shaker. An accelerometer was used to monitor the acceleration of the shaker, which was kept constant at $1m/s^2$ during the slow sinusoidal sweep performed by tuning the amplifier. The harvester delivers its power to a resistor R. A current DAQ card was used to log the root mean square value of current, I_{rms}. The average power delivered to the resistor was calculated by:

$$P_{avg} = I_{rms}^2 R \tag{25}$$

Table 1: Physical and geometric properties of the cantilever beam and the tip body

E_s	Aluminum Young's Modulus (GN/m^2)	69.5
E_p	Piezoelectric material (MFC) Young's Modulus (GN/m^2)	30.336
ρ_s	Aluminum density (kg/m^3)	2700
ρ_p	Piezoelectric material density (kg/m^3)	5440
L	Length of the beam (mm)	62.5
L_1	Left of the beam to starting of the piezoelectric layer (mm)	0
L_2	Left of the beam to ending of the piezoelectric layer (mm)	28
b_1	Width of the aluminum layer (mm)	10
b_2	Width of the piezoelectric layer (mm)	7
h_s	Aluminum layer thickness (mm)	0.6
h_p	Piezoelectric layer thickness (mm)	0.2
M_t	Tip mass (g)	4.64
L_{struc}	Length of the tip mass (mm)	15
b_{struc}	Thickness of the tip mass (mm)	9.4
d_{31}	Strain coefficient of piezoelectric layer (pC/N)	-170
ϵ_{33}^s	Permittivity component at constant strain (nF/m)	12.653
ξ	Mechanical damping ratio	0.00878

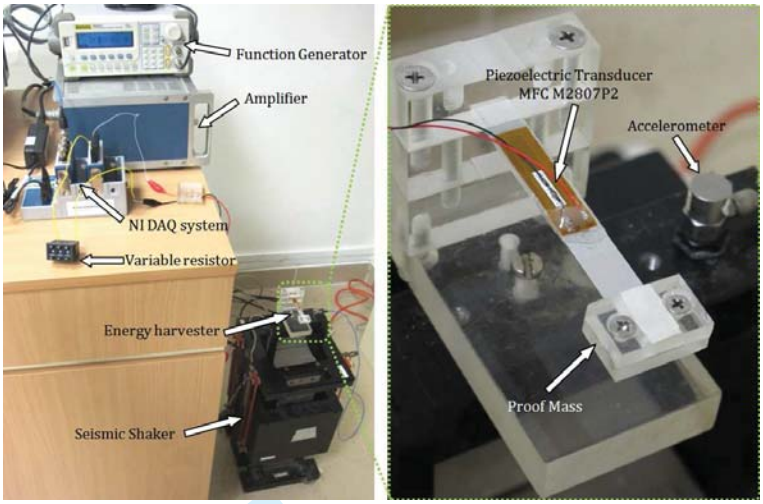

Figure 4: Experimental setup

3. Linear analysis and determination of the optimum load resistance

3.1. Effects of the load resistance on the natural frequency and damping

The effects of the electrical load resistance on the natural frequency and damping of the harvester are determined from a linear analysis of the coupled electromechanical problem. Introducing the following state variables:

$$\mathbf{X} = \begin{bmatrix} X_1 \\ X_2 \\ X_3 \end{bmatrix} = \begin{bmatrix} q \\ \dot{q} \\ V \end{bmatrix}, \tag{26}$$

the equations of motion are rewritten as

$$\dot{X}_1 = X_2 \tag{27}$$

$$\dot{X}_2 = -2\xi\omega X_2 - \omega^2 X_1 - \chi X_3 \tag{28}$$

$$\dot{X}_3 = -\frac{1}{RC_p}X_3 + \frac{\chi}{C_p}X_2 \tag{29}$$

Clearly, these equations have the form

$$\dot{\mathbf{X}} = B\mathbf{X} \tag{30}$$

where

$$B = \begin{bmatrix} 0 & 1 & 0 \\ -\omega^2 & -2\xi\omega & -\chi \\ 0 & \frac{\chi}{C_p} & -\frac{1}{RC_p} \end{bmatrix}.$$

The matrix B has a set of three eigenvalues λ_i, $i = 1, 2, 3$. The first two eigenvalues are similar to those of a pure beam-mass system in the absence of the piezoelectricity effect. The third eigenvalue λ_3 is a result of the electromechanical coupling and is always real and negative. The first two eigenvalues are complex conjugates ($\lambda_2 = \overline{\lambda_1}$). The real part of these eigenvalues represents the electromechanical damping coefficient and the positive imaginary part corresponds to the global frequency of the coupled system.

Inspecting the matrix B, we note that the electrical load resistance has an effect on the overall damping and frequency of the system. Figure 5(a) shows the variation of the global frequency with the electrical load resistance. The global frequency is approximately equal to 175.2 rad/s (27.88 Hz) when the load resistance is set equal to 10^2 Ω; we refer to this frequency as the short global frequency. Increasing the load resistance results in an increase in the global frequency to a value near 176.4 rad/s (28.07 Hz) when the load resistance is near R = 10^8 Ω; we refer to this frequency as the open global frequency. The significant increase from 175.2 rad/s to 176.4 rad/s takes place when the load resistance is increased from near 10^5 Ω to near

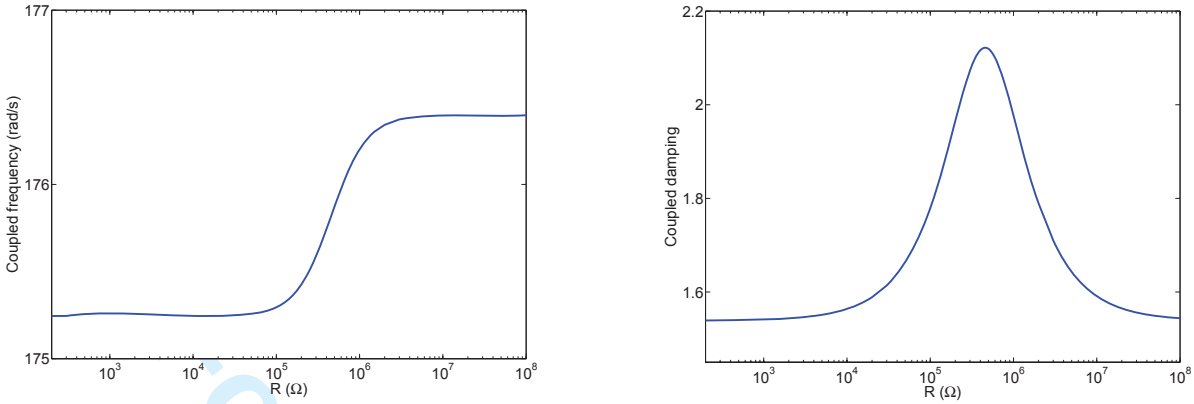

(a) (b)

Figure 5: Variations of the (a) global natural frequency and (b) global coupled damping with the electrical load resistance when L_2=28 mm (experiment prototype).

10^6 Ω. As for the electromechanical damping, inspecting Figure 5(b), we note that the electromechanical damping is maximum for specific values of the load resistance. The region of load resistance over which the electromechanical damping is relatively high coincides with the region over which a significant increase in the global frequency occurs. Away from this region, the electromechanical damping coefficient is relatively smaller.

3.2. Determination of the optimum load resistance

Based on the derived analytical model, we plot respectively in Figures 6(a), (b), and (c) the frequency-response curves of the displacement, generated voltage, and harvested power when varying the load resistance. The variations of the tip displacement with the load resistance is negligible with minimum values obtained when the load resistance is in the range between 10^5 Ω and 10^6 Ω, as shown in Figure 6(a). This is expected because the

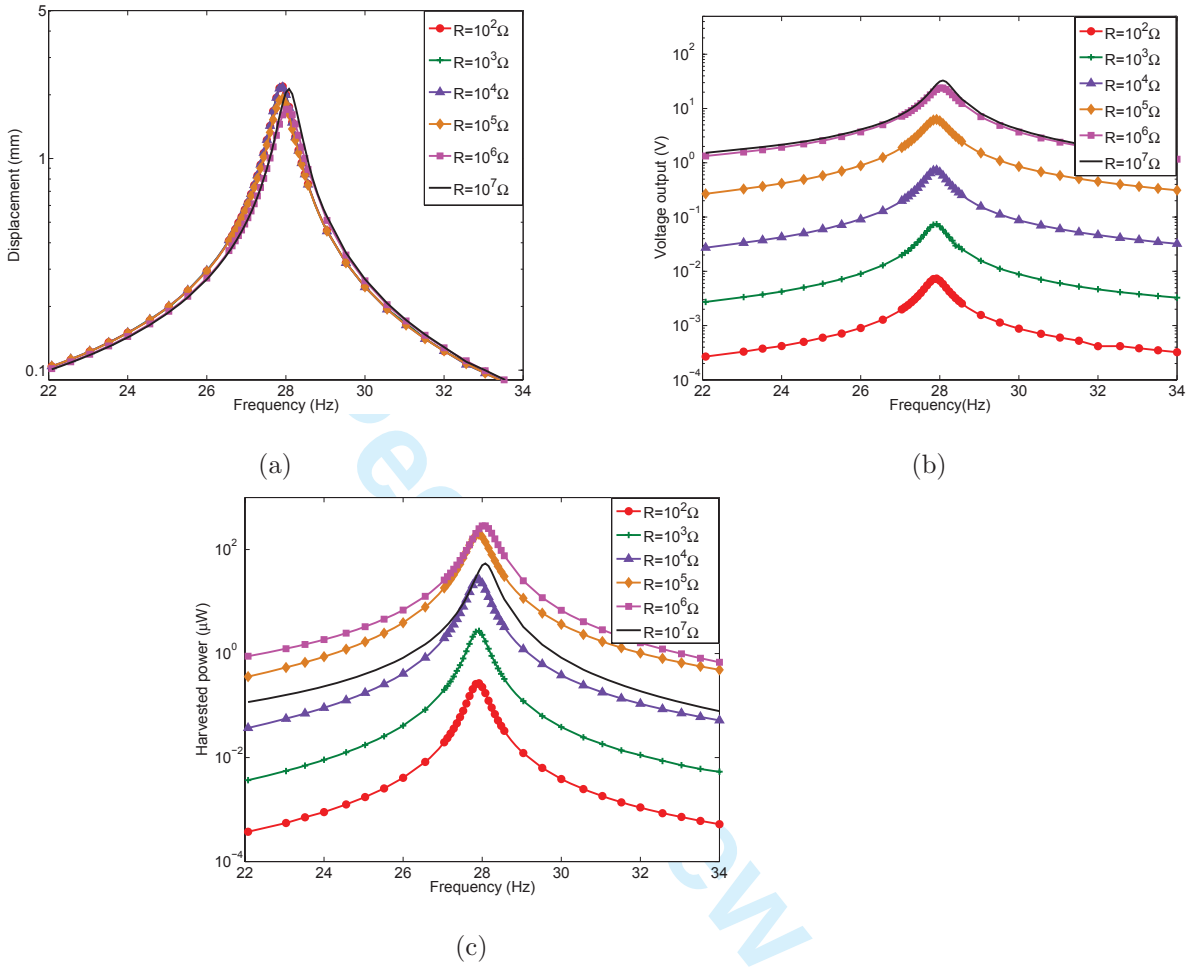

Figure 6: Frequency-response curves of the (a) tip displacement, (b) generated voltage, and (c) harvested power for different values of the electrical load resistance when L_2=28 mm and when $a_{rms} = 1\ m/s^2$.

global electromechanical damping is maximum in this range. Furthermore, inspecting Figure 6(b), we note that increasing the load resistance is accompanied by an increase in the generated voltage and a slight shift in the global frequency. On the other hand, increasing the load resistance is not accompanied with an increase in the harvested power, as shown in Figure 6(c). These results are more clear in the plotted curves of Figure 7 which show the tip displacement, generated voltage, and harvested power for the short- and open-circuit configurations. The short- and open-circuit configurations are defined by matching the excitation frequency Ω with the short and open global frequencies, respectively. As mentioned above, minimum values of the tip displacement are obtained when the global damping is maximized, as shown in Figure 7(a). These minimum displacement values are obtained for load resistance values between 10^5 Ω and 10^6 Ω for both short- and open-circuit configurations. In the lower range ($R < 10^4$ Ω) and higher range ($R > 10^7$ Ω), the variation of the tip displacement with the load resistance is relatively small. It follows from Figure 7(b) that the generated voltage always increases when the load resistance is increased and then reaches a constant value for both configurations. However, there is an optimum value of the load resistance for which the harvested power is maximized. This optimum value depends on the considered configuration and is larger in the case of the open-circuit configuration. We also note that maximum levels of harvested power are accompanied with minimum levels of the tip displacement which occur when the load resistance is between 10^5 Ω and 10^6 Ω. More accurately, maximum levels of harvested power are obtained when the electrical load resistance is almost equal to 4×10^5 Ω.

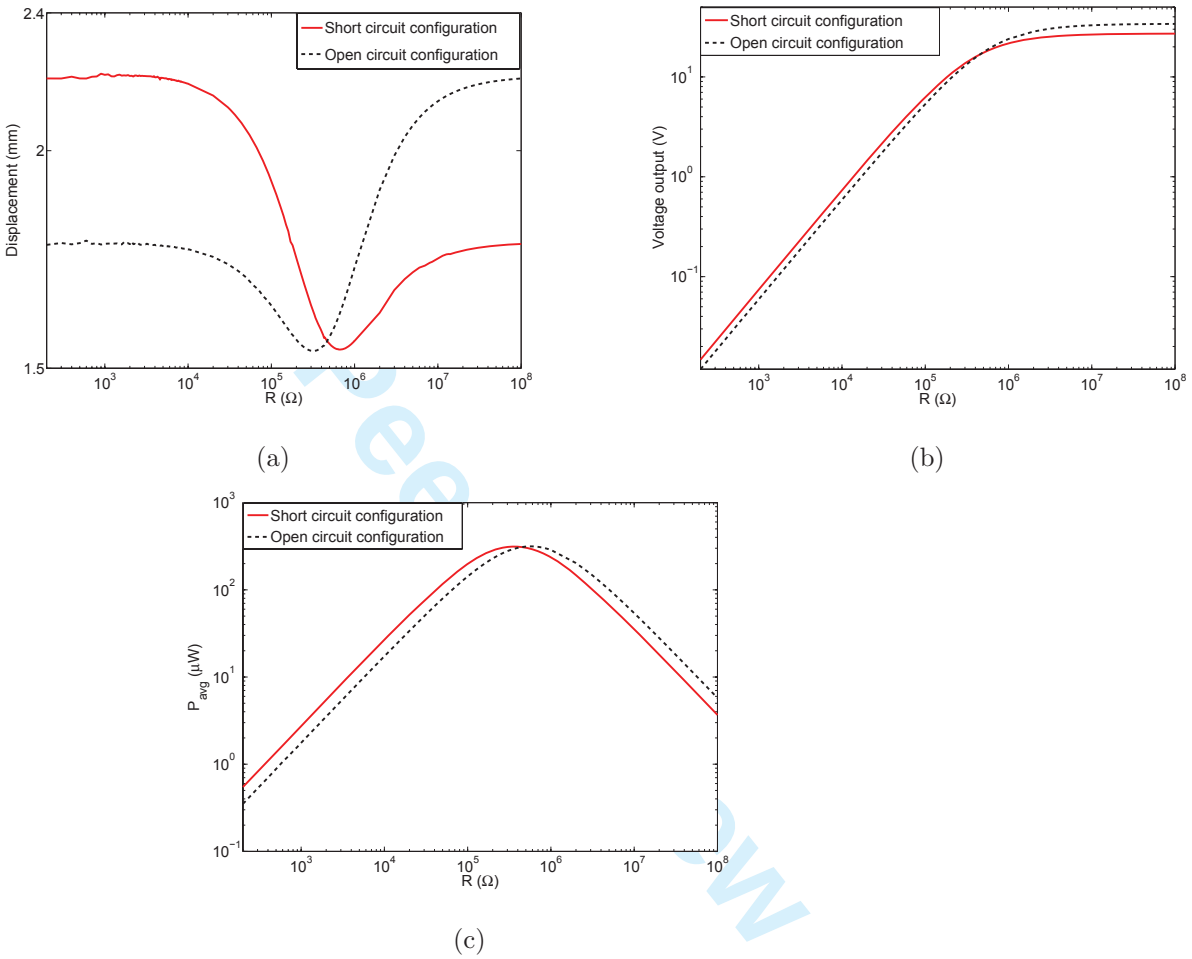

Figure 7: (a) Tip displacement, (b) generated voltage, and (c) harvested power when L_2=28 mm and when $a_{rms} = 1m/s^2$ for the short- and open-circuit configurations.

4. Experimental measurements and models validation

A comparison of the short and open global frequencies obtained from the analytical and finite element analysis with the experimental measurements is presented in Table 2. The values show that the short and open global frequencies of the derived analytical model and finite element electromechanical model are in good agreement ($< 3\%$) with the experimental results. On the other hand, there is a discrepancy in the short and open frequencies obtained by using the approximate model and experimental measurements. In fact, the approximated model overestimates the values of these two global frequencies. This overestimation can lead to erroneous results when performing the frequency-response analysis and short and open-circuit configurations or if an approximate model is used to design an energy harvester.

Table 2: Short and open global frequencies: comparisons between different models and experimental measurements.

	Short frequency (Hz)	% difference	Open frequency (Hz)	% difference
Experiment	27.8	–	28	–
Derived model	27.88	0.29	28.07	0.25
Approximated model	28.31	1.8	29	3.6
FEA (ANSYS)	27.79	0.035	27.97	0.11

In Figure 8, we plot the frequency-response curves of the average harvested power as obtained from the different models and the experimental measurements when the load resistance is set equal to the optimal value (R=$4 \times 10^5 \Omega$) and when the root mean square of the base acceleration is set equal to 1 m/s^2. The plots show that the derived analytical model ac-

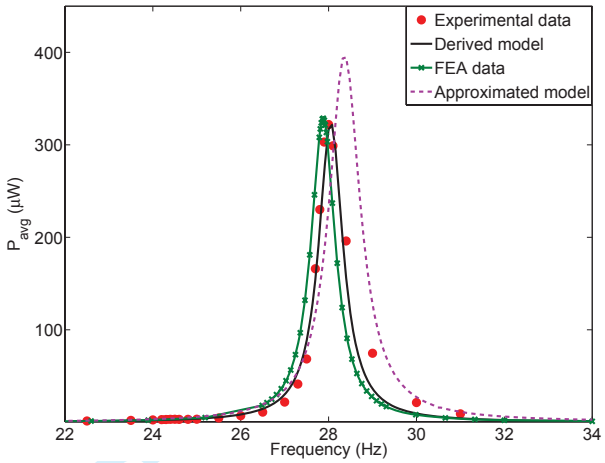

Figure 8: Comparisons of the frequency-response curves between the used models and experimental measurements when $a_{rms} = 1m/s^2$.

curately predicts the experimental measurements. The finite element results are generally in good agreement. There is a small discrepancy in the global frequency of the harvester and slight overestimation of the value of the harvested power at resonance. On the other hand, the approximated analytical model overestimates both the global frequency and the level of harvested power.

Figure 9 shows variations of the average harvested power with the load resistance as predicted from the analytical models and finite element model, and measured experimentally. The analytical derived model and finite electromechanical model accurately predict the response of the harvester for both the short- and open-circuit configurations. On the other hand, the analytical approximate model significantly underestimates or overestimates the power level over a broad range of the resistance values. The above comparisons and validations show that the analytically derived and finite element electrome-

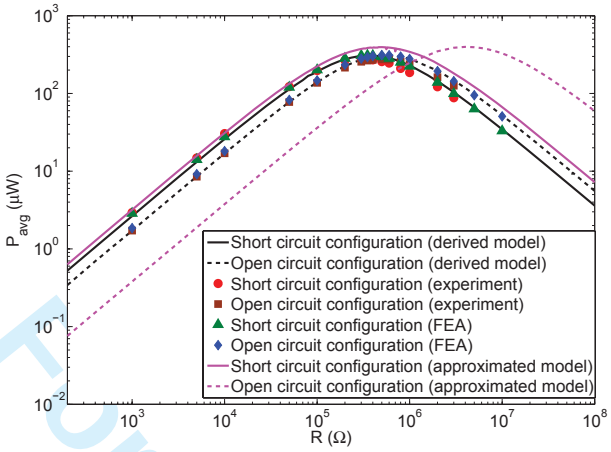

Figure 9: Comparisons of the short- and open-circuit configurations between the used models and experimental measurements when $a_{rms} = 1\ m/s^2$.

chanical models give more accurate results when compared to the analytical approximate model. Because the use of the analytical derived model is more flexible and computationally inexpensive than the finite element model, we will use it in the following section to design enhanced piezoelectric energy harvesters with smaller volumes that have higher power densities.

5. Piezoelectric material length effects on the behavior of the harvester: Tunability

5.1. Effects of the piezoelectric material length on the natural frequencies and mode shapes

One of the most interesting parameters that can affect the performance of the harvester is the length of the attached piezoelectric material. Changing this length results in a variation in the capacitance of the harvester, the piezoelectric coupling, the natural frequency, the mode shape, and the forcing

term. Consequently, all associated terms in equations (22) and (23) will be changed and new analyses must be performed. We start by determining the effects of varying the length of the piezoelectric material on the natural frequency and associated mode shape. This investigation is performed for two different system parameters. The first one has the same parameters as those of the experimental prototype except for the length of the piezoelectric sheet (L_2) which is varied systematically. We refer to this configuration as the first energy harvesting system. In the second configuration, we change the length of the aluminum beam to 70 mm, the thickness and width of the piezoelectric sheet to 0.356 mm and 1 cm, respectively, and the tip mass to 4.52 g. We refer to this configuration as the second energy harvesting system.

Figure 10(a) shows variations of the natural frequency of these two systems with the length of the piezoelectric sheet. The plots show that decreasing the length of the piezoelectric material results in a decrease in the value of the natural frequency for both systems. This is beneficial in terms of managing low frequency excitations for piezoelectric energy harvesters and enhancing their power densities. Furthermore, there is an optimum value of the piezoelectric length beyond which the natural frequency could not be increased significantly. This value is near 53 mm for the first system and 60 mm for the second system. However, for small length values of the piezoelectric sheet, the rate of variation of the natural frequency with L_2 is important. Based on this analysis and depending on the available excitation frequency, the harvester can be passively tuned to match its natural frequency to the available excitation frequency. Figures 10(b) and 10(c) show variations of the first mode shape with the length of the piezoelectric sheet for both systems,

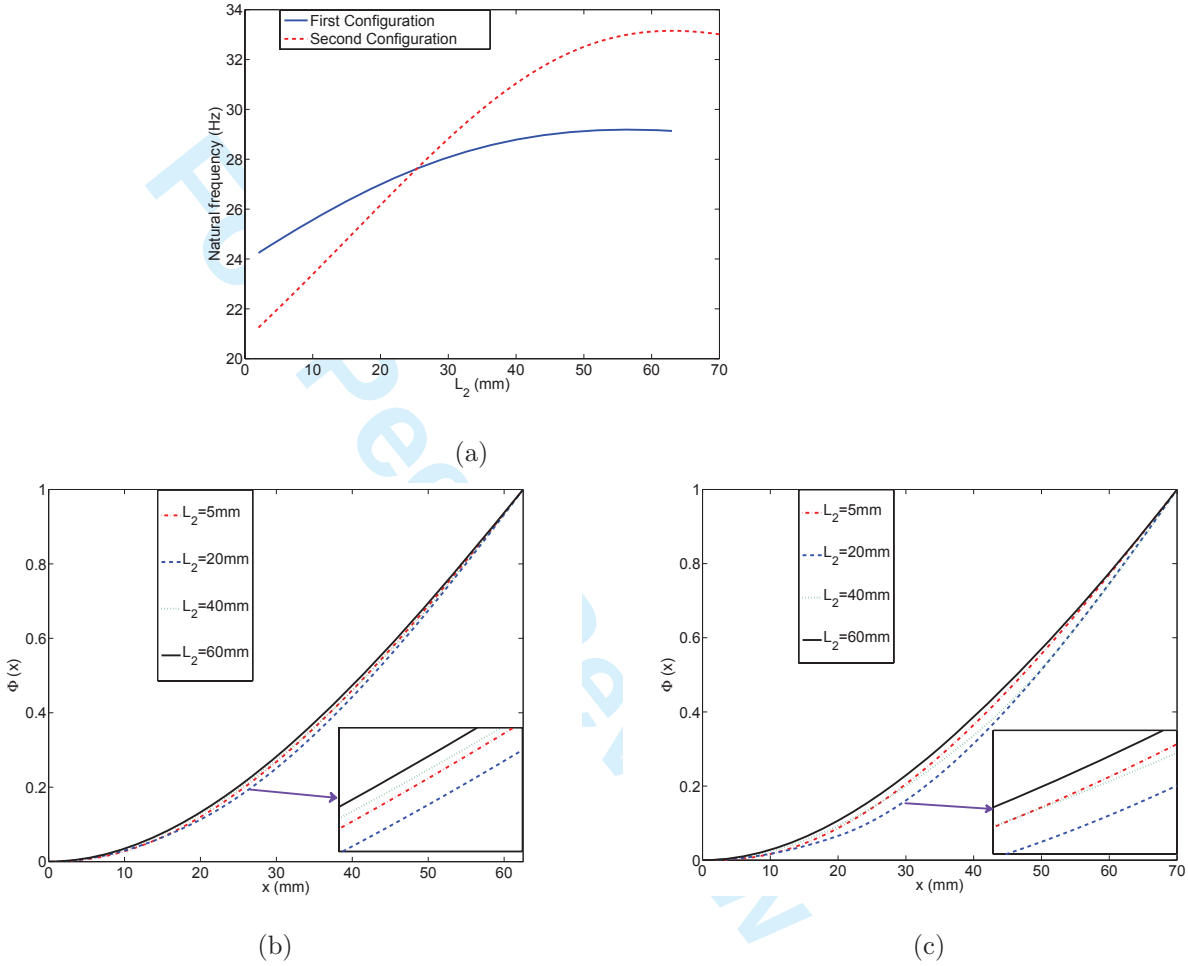

Figure 10: Variations of the (a) structural natural frequency and (b,c) mode shapes with the length of the piezoelectric material for the first and second systems.

respectively. The plots show that there is a significant change in the mode shape when varying the length of the piezoelectric sheet. The difference between the mode shapes varies depending on this length.

5.2. Effects of the piezoelectric material length on the performance of the harvester

The plots in Figures 11 and 12 show the frequency-response curves of the harvested power when varying the length of the piezoelectric material for different values of the electrical load resistance. The plots show that the level of the harvested power is significantly affected by the length of the piezoelectric sheet as well as the load resistance. The frequency-response curves of the first system when the length of the piezoelectric sheet is set equal to 50 mm and 60 mm are very close to each other. In addition, for the same system and when $R = 10^5\ \Omega$ and $R = 10^6\ \Omega$, the maximum (resonant) values of the harvested power are very close when the length of the piezoelectric sheet is set equal to 30 mm, 40 mm, 50 mm, and 60 mm. In the second system, the same behavior is observed. Furthermore, for both systems, there is a compromise between the length of the piezoelectric material, the electrical load resistance, and the available excitation frequency that leads to maximum levels of harvested energy.

To investigate more this compromise, we plot in Figures 13 and 14 variations of the resonant average harvested power with the load resistance and length of the piezoelectric material and for both systems, respectively. It follows from Figures 13(a) and 14(a) that there is an optimum value of the load resistance for which the resonant value of the harvested power is maximized for all considered piezoelectric lengths. We note also that this region is

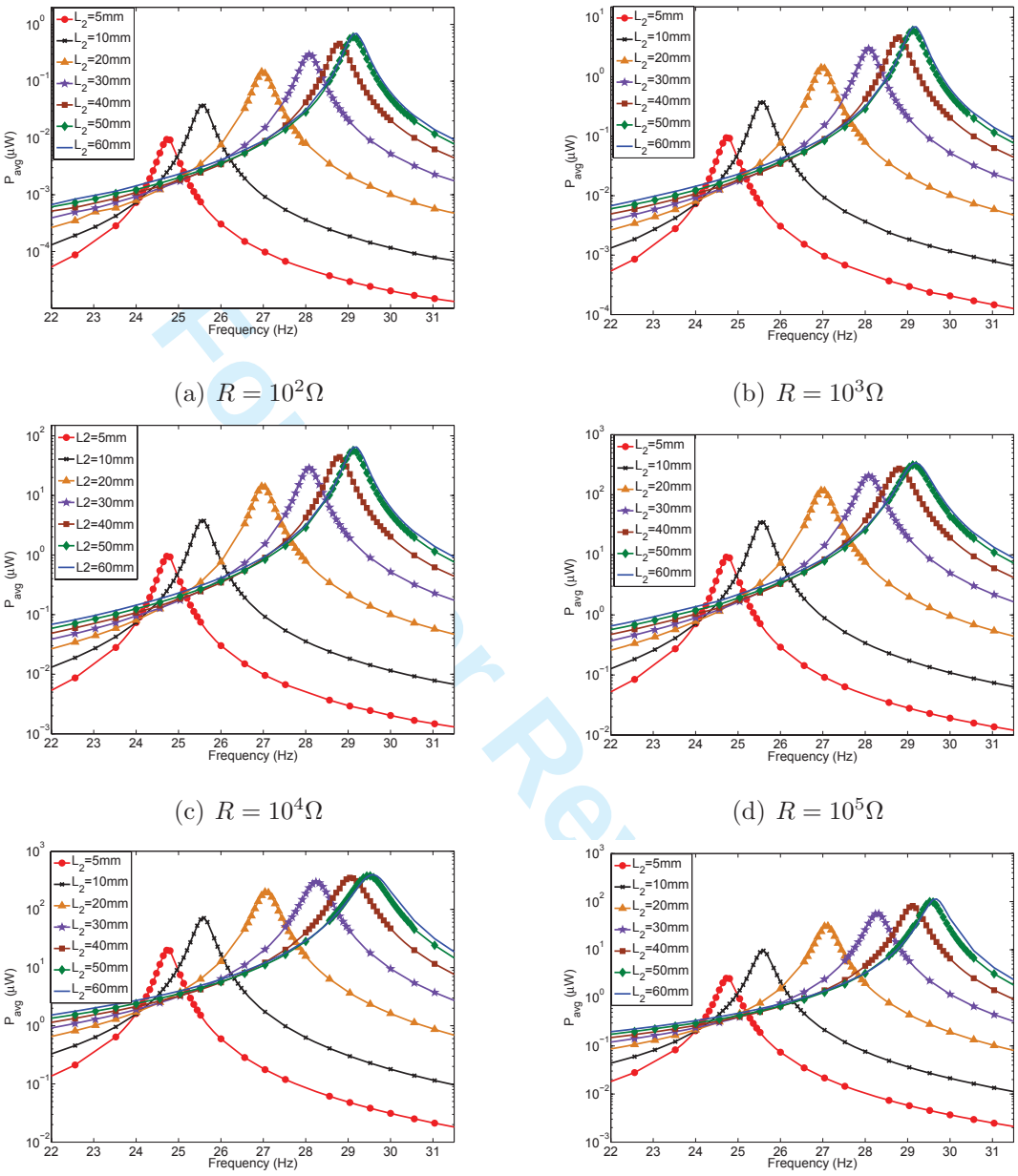

(a) $R = 10^2\Omega$ (b) $R = 10^3\Omega$

(c) $R = 10^4\Omega$ (d) $R = 10^5\Omega$

(e) $R = 10^6\Omega$ (f) $R = 10^7\Omega$

Figure 11: Variations of the average harvested power with the length of the piezoelectric material for different load resistances and for the first system when $a_{rms} = 1\ m/s^2$.

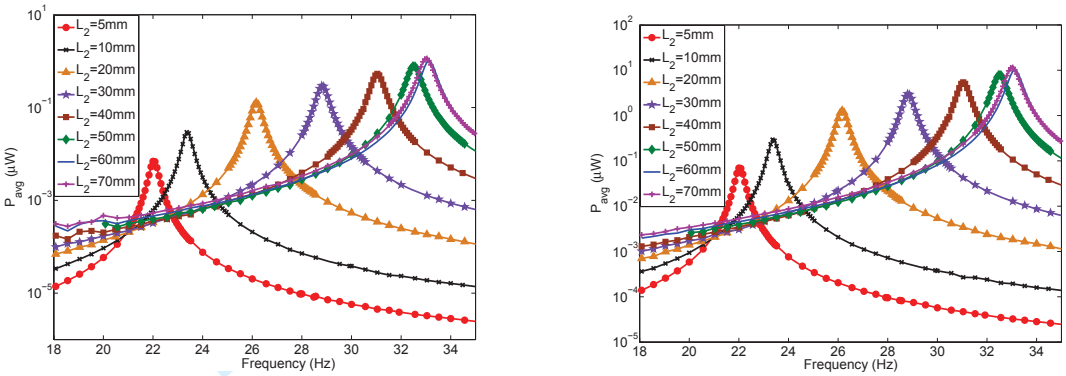

(a) $R = 10^2\Omega$ (b) $R = 10^3\Omega$

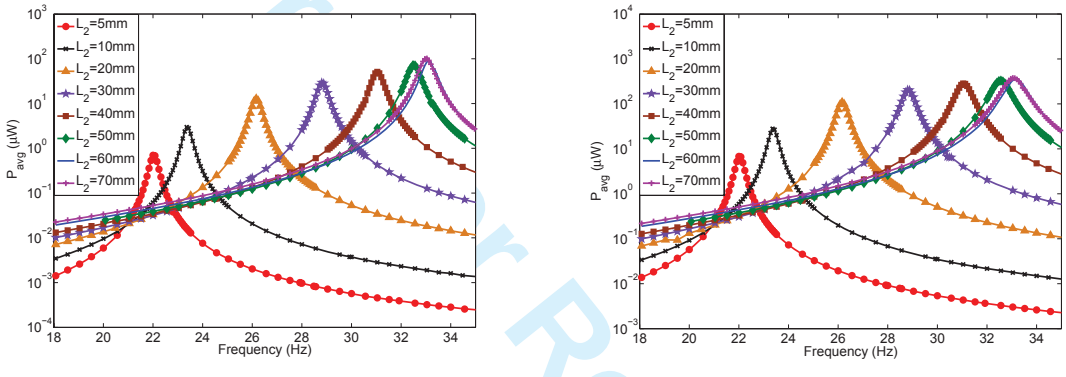

(c) $R = 10^4\Omega$ (d) $R = 10^5\Omega$

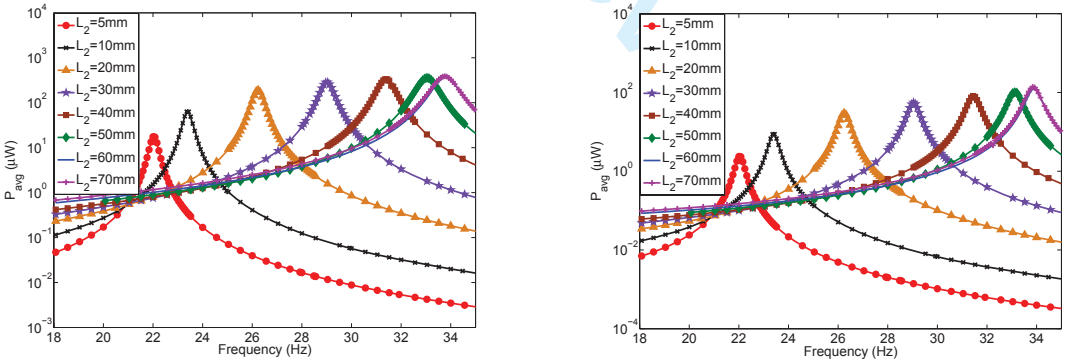

(e) $R = 10^6\Omega$ (f) $R = 10^7\Omega$

Figure 12: Variations of the harvested power with the length of the piezoelectric material for different load resistances and for the second system when $a_{rms} = 1\ m/s^2$.

almost the same for both systems. In the first system, increasing the length of the piezoelectric material is accompanied with an increase in the value of the resonant harvested power. The rate of increase of the harvested power is important when the length of the piezoelectric sheet is increased from 5 mm to 30 mm. Beyond 30 mm, this rate becomes very small, as shown in Figure 13(b). In the second system, increasing the length of the piezoelectric sheet is followed by an increase in the average harvested power and then stabilizes at higher piezoelectric length values. In addition, the rate of increase of the harvested power is significantly affected by the length of the piezoelectric sheet when its length is between 5 mm and 20 mm. At higher values, the variation rate of the harvested power becomes very small. Consequently, we can conclude that depending on the excitation frequency, an enhanced harvester can be designed by changing the length of the piezoelectric material and the electrical load resistance.

5.3. Effects of the length of the piezoelectric sheet on the short- and open-circuit configurations

As mentioned above, the length of the piezoelectric sheets affects the natural frequency, the mode shape, the capacitance of the harvester, and the piezoelectric coupling. Because the values of the short and open global frequencies depend on the harvester's parameters, we present in Table 3 the values of these frequencies for both systems and for different lengths of the piezoelectric sheet. We note that the difference between the open and short frequencies is negligible for small values of the piezoelectric material length. Furthermore, increasing the length of the piezoelectric material is accompanied with an increase in the difference between these frequencies.

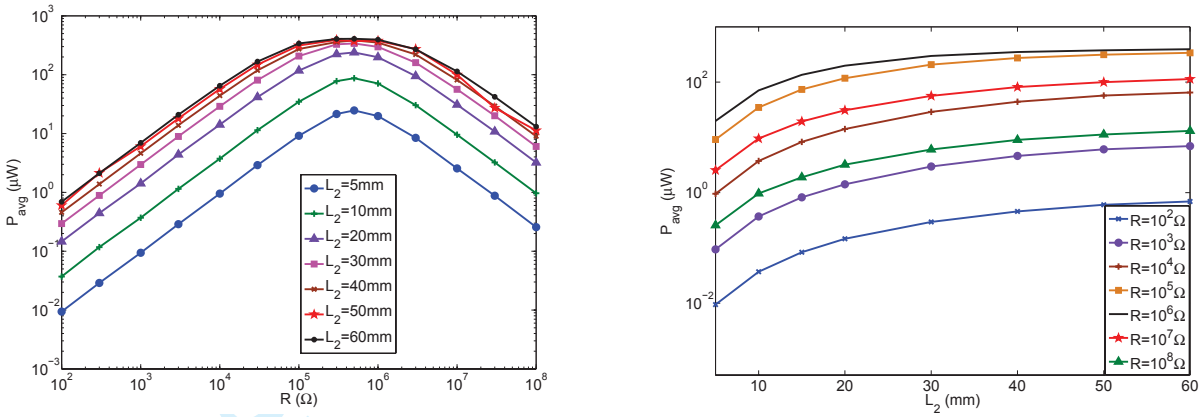

(a) (b)

Figure 13: Variations of the resonant average harvested power with (a) the load resistance and for different piezoelectric lengths and (b) the length of the piezoelectric material for different load resistances when $a_{rms} = 1\ m/s^2$ and for the first system.

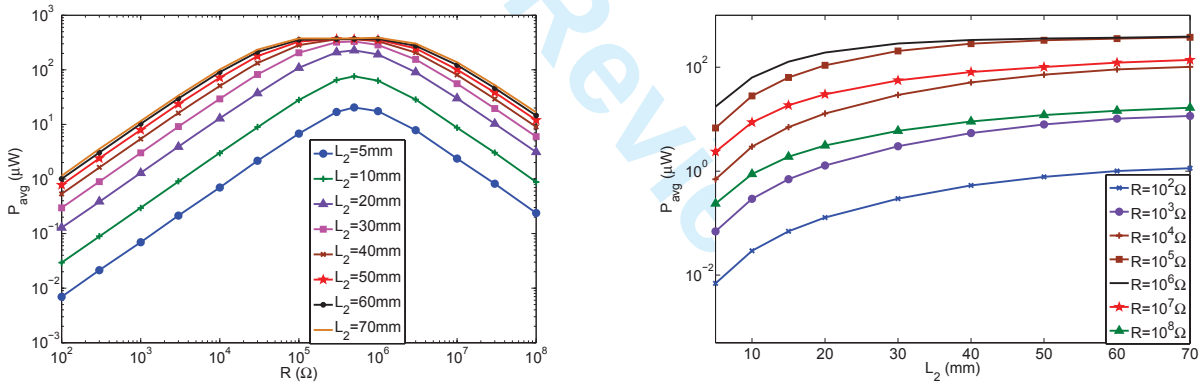

(a) (b)

Figure 14: Variations of the resonant average harvested power with (a) the load resistance and for different piezoelectric lengths and (b) the length of the piezoelectric material for different load resistances when $a_{rms} = 1\ m/s^2$ and for the second system.

Table 3: Short and open global frequencies for different lengths of the piezoelectric sheet and for both systems.

$L_2(mm)$	$w_s(Hz)$ (first)	$w_o(Hz)$ (first)	$w_s(Hz)$ (second)	$w_o(Hz)$ (second)
5	24.75	24.756	22.033	22.037
10	25.561	25.586	23.385	23.402
20	26.989	27.086	26.161	26.247
30	28.079	28.286	28.822	29.042
40	28.785	29.112	31.039	31.453
50	29.124	29.552	32.509	33.129
60	29.165	29.656	33.12	33.897
70	–	–	33.011	33.863

We plot in Figures 15(a) and (b) the average harvested power using short- and open-circuit configurations of both the first and second systems. We note that the short- and open-circuit configurations when $L_2 = 10\ mm$ are the same. This is expected because the short and open frequencies are almost the same, as shown in Table 3. In addition, increasing the length of the piezoelectric sheet is accompanied with a significant distinction between the short- and open-circuit configurations. For $L_2 = 40\ mm$ and $L_2 = 60\ mm$, we note that, depending on the region of the considered load resistance and the short- or open-circuit configuration, the average harvested power can be higher when $L_2 = 40\ mm$ or higher when $L_2 = 60\ mm$. For example, when the load resistance is set equal to $10^3\ \Omega$ and for the short-circuit configuration, the average value of the harvested power is higher when $L_2 = 60\ mm$ than $L_2 = 40\ mm$. On the other hand, when changing the value of the load resistance to $10^7\Omega$, the average value of the harvested power is higher when

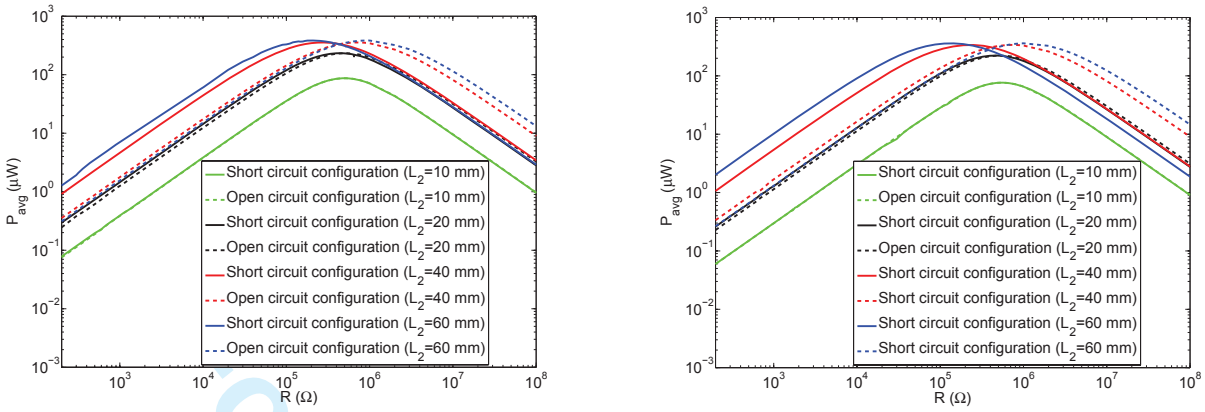

Figure 15: Variations in the average harvested power using short- and open-circuit configurations for different length of the piezoelectric material and for (a) the first system and (b) the second system and when $a_{rms} = 1\ m/s^2$.

$L_2 = 40mm$ than $L_2 = 60\ mm$. We conclude that depending on the available excitation frequency, there is a compromise between the load resistance and the length of the piezoelectric sheet to get enhanced levels of harvested power.

6. Conclusions

We have developed analytical and finite element electromechanical models that take into account the fact that the piezoelectric sheet does not cover the whole substrate beam of a beam-mass energy harvester. In addition, we used the approximate electromechanical model that is based on the classical mode shapes (fully-covered beam) in the Galerkin discretization. A linear analysis of the derived analytical model was performed to determine the optimal load resistance. By comparing results from the derived analytical

models and finite element analysis results with experimental measurements, we determined that a model which uses mode shapes that are based on the length of the piezoelectric sheet are better suited than approximate models that are based on a fully covered beam to predict the performance of the harvester. The results showed that the finite element results gives a slight discrepancy in the global frequency of the harvester and harvested power at resonance. In orde to design enhanced piezoelectric energy harvesters that can generate energy at low frequency excitations, a parametric study based on the analytical derived model was then performed to investigate the effects of the length of the piezoelectric sheet on the natural frequency and level of harvested power. The results showed that depending on the available low excitation frequency an enhanced piezoelectric energy harvester can be tuned and optimized by changing the length of the piezoelectric sheet and load resistance.

References

Abdelkefi, A., Najar, F., Nayfeh, A. H., Ben Ayed, S. 2011,"An energy harvester using piezoelectric cantilever beams undergoing coupled bending-torsion vibrations," *Smart Materials and Structures* 20, 115007.

Abdelkefi, A., Nayfeh, A. H. and Hajj, M. R. 2012. "Modeling and analysis of piezoaeroelastic energy harvesters," *Nonlinear Dynamics* 67, 925-939.

Abdelkefi, A., Hajj, M. R. and Nayfeh, A. H. 2012. "Sensitivity analysis of piezoaeroelastic energy harvesters," *Journal of Intelligent Material Systems and Structures* 23, 1523–1531.

Abdelkefi, A., Nayfeh, A. H., Hajj, M. R., and Najar, F. 2012, "Energy harvesting from a multifrequency response of a tuned bendingtorsion system," *Smart Materials and Structures* 20, 075029.

Abdelkefi, A., Yan, Z. and Hajj, M. R. 2013. "Performance analysis of galloping-based piezoaeroelastic energy harvesters with different cross-section geometries," *Journal of Intelligent Material Systems and Structures* DOI: 10.1177/1045389X13491019.

Alamin Dow, A. B., Schneider, M., Koo, D., Al-Rubaye, H. A., Bittner, A., Schmid, U. and Kherani, N. 2012. "Modeling the performance of a micromachined piezoelectric energy harvester," *Microsystem Technologies* 18, 10351043.

Ben Ayed, S., Abdelkefi, A., Najar, F. and Hajj, M. R. 2013. "Design and performance of variable-shaped piezoelectric energy harvesters," *Journal of Intelligent Material Systems and Structures* DOI: 10.1177/1045389X13489365.

Daqaq, M. F. 2012. "On intentional introduction of stiffness nonlinearities for energy harvesting under white Gaussian excitations," *Nonlinear Dynamics* 69, 1063-1079.

DuToil, N. E., Wardle, B. L. and Kim, S. G. 2005. "Design considerations for MEMS-scale piezoelectric mechanical vibration energy harvesters," *Integrated Ferroelectric* 71, 121-60.

Erturk, A., Vieira, W. G. R., De Marqui, C. and Inman, D. J. 2010. "On the

energy harvesting potential of piezoaeroelastic systems," *Applied Physics Letters* 96, 184103.

Erturk, A. and Inman, D. J. 2008. "On mechanical modeling of cantilevered piezoelectric vibration energy harvesters," *Journal of Intelligent Material Systems and Structures* 19, 1311–1325.

Erturk, A. and Inman, D. J. 2008. "A distributed parameter electromechanical model for cantilevered piezoelectric energy harvesters," *ASME Journal of Vibration and Acoustics* 130, 041002.

Erturk, A. and Inman, D. J. 2009. "An experimentally validated bimorph cantilever model for piezoelectric energy harvesting from base excitations," *Smart Materials and Structures* 18, 025009.

Hobeck, J. D. and Inman, D. J. 2012 Artificial piezoelectric grass for energy harvesting from turbulence-induced vibration," *Smart Materials and Structures* 21, 105024.

IEEE. 1987. "Standard on Piezoelectricity".

Karami, M. A. and Inman, D. J. 2011. "Analytical modeling and experimental verification of the vibrations of the zigzag microstructure for energy harvesting," *Journal of Vibration and Acoustics* 133, 011002.

Masana, R. and Daqaq, M. F. 2011. "Electromechanical modeling and nonlinear analysis of axially loaded energy harvesters," *ASME Journal of Vibration and Acoustics* 133, 1–10.

Roundy, S. and Wright, P. K. 2005. "A piezoelectric vibration-based generator for wireless electronics," *Journal of Intelligent Material Systems and Structures* 16, 809–823.

Song, H. J., Choi, Y-T., Purekar, A. S. and Wereley, N. M. 2009. "Performance evaluation of multi-tier energy harvesters using macro-fiber composite patches," *Journal of Intelligent Material Systems and Structures* 20, 2077–2088.

Song, H. J., Choi, Y-T., Wereley, N. M. and Purekar, A. S. 2010. "Energy harvesting devices using macro-fiber composite materials," *Journal of Intelligent Material Systems and Structures* 21, 647–658.

Sousa, V. C., Anicezio, M de M, De Marqui, C. and Erturk, A. 2011. "Enhanced aeroelastic energy harvesting by exploiting combined nonlinearities: theory and experiment," *Smart Materials and Structures* 20, 094007.